ISSN 0915-633X

NATIONAL INSTITUTE FOR FUSION SCIENCE

An Advanced Electrostatic Particle Simulation Algorithm for Implicit Time Integration

T.H. Watanabe, Y. Todo, R. Horiuchi, K. Watanabe, T. Sato

(Received - Nov. 15, 1994)

NIFS-331 Jan. 1995

RESEARCH REPORT
NIFS Series

NAGOYA, JAPAN

An Advanced Electrostatic Particle Simulation Algorithm for Implicit Time Integration

T.H. Watanabe, Y. Todo, R. Horiuchi, K. Watanabe, T. Sato

Theory and Computer Simulation Center,
National Institute for Fusion Science, Nagoya 464-01, Japan

Abstract

We have developed an advanced electrostatic macro-scale implicit particle simulation code (AMACS-ES), which enables us to simulate low-frequency plasma wave phenomena with large spatial scale length. Especially, the Poisson's equation with the implicit susceptibility term is accurately solved in our algorithm. Linear properties of the simulation code based on this algorithm, such as the linear stability and the dispersion relation, are examined. We have also applied our simulation code to the excitation and nonlinear saturation of the ion temperature gradient (ITG) drift instability in a system with a shearless slab geometry. The linear properties of the excited ITG mode are compared with the theoretical prediction to find a good agreement.

Key words :

Electrostatic plasma, Particle simulation, Implicit time integration

1 Introduction

In the last three decades, the particle simulation method has been employed for studying nonlinear plasma waves with kinetic effects such as the Landau and cyclotron dampings. While various nonlinear plasma phenomena have been clarified by the conventional particle simulation with explicit time integration, the applicability is limited to high-frequency plasma waves with short wavelengths. This is because the simulation time step Δt should be less than ω_p^{-1} and the grid spacing has to be comparable to the Debye length [1,2]. Thus, it is difficult to study kinetic waves with MHD space and time scales by means of the conventional particle simulation method. In fusion and space plasmas, however, one notices the importance of kinetic effects on MHD and transport scale phenomena, such as the excitation of MHD waves by high energy (alpha) particles, anomalous heat transport caused by drift waves, triggering of collisionless reconnection and so on. For the purpose of obtaining a feasible tool that can be useful for the study of the nonlinear plasma dynamics with large space and time scales, many efforts have been made to overcome the technical restriction pertinent to the conventional particle simulation. The direct implicit particle simulation technique has been developed and improved by continuous efforts over the last decade [1-4]. In the direct method, a time-filtered equation of motion for each particle, which is numerically stable against the high-frequency plasma oscillation, is solved along with the Poisson's equation which is modified with the implicit susceptibility term.

The algorithm of the macro-scale particle simulation code [5] is essentially a direct implicit method. The featuring point of this algorithm is to use a time-decentering scheme for integrating the equation of motion and the Maxwell's equations instead of the time-filtering technique in the direct method. Eigenmodes of the electromagnetic waves in the macro-scale algorithm were in good agreement with the theoretical dispersion relations of the Alfvén wave and the whistler mode wave [5]. Electrostatic modes propagating along with the magnetic field, however, exhibit a broad-band nature, thus, no significant peak is recognizable in the power spectrum of the ion acoustic branch (see Fig.6 in Ref.[5]). Therefore, we need to find feasibility of an electrostatic macro-scale particle simulation algorithm with low-noise level and high-accuracy.

In this paper, we will give an electrostatic version of the revised macro-scale particle

simulation algorithm (AMACS-ES), and will check the validity of our method both analytically and numerically. The implicit Poisson's equation is needed to solve even in the electromagnetic particle simulation in order to satisfy the charge continuity law. Thus, the electrostatic characteristics obtained in this study can be applied to the electromagnetic case, as well. The numerical algorithm will be described in section 2. In section 3, we will make stability analysis of our simulation scheme using the procedure given by Langdon [6], and will check the numerical accuracy of the electrostatic field calculation. Simulation results will be shown in section 4, where the ion temperature gradient (ITG) drift instability will be examined by its two-dimensional version including the effect of the polarization drift [7]. Summary and discussion will be given in section 5.

2 Simulation Algorithm

2.1 Electrostatic Algorithm in 1-D System

For the time being let us consider an unmagnetized electrostatic plasma in one-dimensional system. In AMACS-ES, the equation of motion for each particle i with a shape function $S(x)$ is given by [5]

$$x_i^{n+1} = x_i^n + \Delta t v_i^n + \frac{q_i \Delta t^2}{2m_i} \sum_j \Delta x S(X_j - \bar{x}_i^{n+\alpha}) E_j^{n+\alpha} , \quad (1)$$

$$v_i^{n+1} = v_i^n + \frac{q_i \Delta t}{m_i} \sum_j \Delta x S(X_j - \bar{x}_i^{n+\alpha}) E_j^{n+\alpha} , \quad (2)$$

where x_i^n and v_i^n are a particle position and velocity at the n-th time step; q_i and m_i denote the charge and mass of the particle; X_j means the position of a grid point and the suffix j indicates the grid number. The time-decentering parameter α is in the range of $0.5 \leq \alpha \leq 1$. When $\alpha = 0.5$, Eqs.(1) and (2) are time-centered. As is given in the above equations, the electric field $E^{n+\alpha}$, which is given by the linear interpolation of $E^{n+\alpha} = \alpha E^{n+1} + (1-\alpha) E^n$, acts on the particle at $x = \bar{x}_i^{n+\alpha}$. Here, $\bar{x}_i^{n+\alpha}$ is provided by $\bar{x}_i^{n+\alpha} = x_i^n + \alpha \Delta t v_i^n$.

As is described in Eqs.(1) and (2), particles are accelerated by E^n and E^{n+1}, while E^{n+1} is unknown at the n-th time step. In the implicit particle algorithm, thus, the Poisson's equation is not solved directly, because the particle position x_i^{n+1}, hence, the charge density $\rho_j(x_i^{n+1})$ has not been obtained at the n-th time step. Therefore, the

Poisson's equation at the $(n+1)$-th time step is approximated by the Taylor expansion at $\tilde{x}_i^{n+1}$,

$$-\nabla^2\phi_j^{n+1} = \rho_j(x_i^{n+1})/\epsilon_0 \tag{3}$$

$$\approx \rho_j(\tilde{x}_i^{n+1})/\epsilon_0 + \delta\rho_j(\tilde{x}_i^{n+1})/\epsilon_0 \tag{4}$$

with

$$\tilde{x}_i^{n+1} = x_i^n + \Delta t v_i^n + (1-\alpha)\frac{q_i\Delta t^2}{2m_i}\sum_j \Delta x S(X_j - \tilde{x}_i^{n+\alpha})E_j^n \ . \tag{5}$$

Here,

$$\rho_j(\tilde{x}_i^{n+1}) = \sum_i q_i S(X_j - \tilde{x}_i^{n+1}) \ , \tag{6}$$

and

$$\delta\rho_j(\tilde{x}_i^{n+1}) = -\nabla\cdot\sum_i \alpha\frac{q_i^2\Delta t^2}{2m_i}S(X_j - \tilde{x}_i^{n+1})\sum_l \Delta x S(X_l - \tilde{x}_i^{n+1})(-\nabla\phi_l^{n+1}) \ . \tag{7}$$

After solving Eq.(4), one can calculate the particle position and velocity at the $(n+1)$-th time step. Conventionally, the implicit term in Eq.(7), which consists of spatial convolution, is further simplified [1,3,5], that is,

$$\delta\rho_j(\tilde{x}_i^{n+1}) \approx -\nabla\cdot\sum_i \alpha\frac{q_i^2\Delta t^2}{2m_i}S(X_j - \tilde{x}_i^{n+1})(-\nabla\phi_j^{n+1}) \ . \tag{8}$$

Note that the second summation on l in Eq.(7) is replaced by $-\nabla\phi_j^{n+1}$. This simplification reduces Eq.(4) to a tri- or penta-diagonal matrix equation of ϕ_j^{n+1}, if $S(x)$ is the *nearest-grid-point* or *linear-interpolation* function. In such a case, we can easily solve Eq.(4) by means of an adequate matrix equation solver.

The present study, however, has disclosed that the approximation in Eq.(8) results in a serious numerical error in association with the inconsistent filtering. Thus, Eq.(7) should be employed without any approximation and Eq.(4) should be solved iteratively. Numerical accuracy of our method will be examined in section 3.

2.2 Electrostatic Algorithm in 2-D System

In a two-dimensional case with an external magnetic field B, particle velocity perpendicular to the magnetic field is given by the E×B drift both for the electrons and ions.

Only parallel velocity $\mathbf{v}_{\|i}^{n+1}$ is calculated from the equation of motion as follows:

$$\begin{aligned}\mathbf{x}_i^{n+1} &= \mathbf{x}_i^n + \Delta t \mathbf{v}_{\|i}^n \\ &+ \sum_{j,k} \Delta x \Delta y S(\mathbf{X}_{jk} - \bar{\mathbf{x}}_i^{n+\alpha}) \left[\frac{\Delta t}{B^2} \mathbf{E}_{jk}^{n+\alpha} \times \mathbf{B} + \frac{q_i \Delta t^2}{2m_i} \mathbf{E}_{\|jk}^{n+\alpha} \right] , \qquad (9) \\ \mathbf{v}_{\|i}^{n+1} &= \mathbf{v}_{\|i}^n + \frac{q_i \Delta t}{m_i} \sum_{j,k} \Delta x \Delta y S(\mathbf{X}_{jk} - \bar{\mathbf{x}}_i^{n+\alpha}) \mathbf{E}_{\|jk}^{n+\alpha} , \qquad (10)\end{aligned}$$

where $\bar{\mathbf{x}}_i^{n+\alpha} = \mathbf{x}_i^n + \alpha \Delta t \mathbf{v}_{\|i}^n$. The Poisson's equation is modified by introducing the polarization term [7]:

$$-\nabla^2 \phi_{jk}^{n+1} - \nabla_\perp \cdot \frac{1}{\epsilon_0 B^2} \sum_i m_i S(\mathbf{X}_{jk} - \mathbf{x}_i^{n+1}) \nabla_\perp \phi_{jk}^{n+1} = \rho_{jk}(\mathbf{x}_i^{n+1})/\epsilon_0 . \qquad (11)$$

The above equation is also expanded at $\tilde{\mathbf{x}}_i^{n+1}$, where

$$\begin{aligned}\tilde{\mathbf{x}}_i^{n+1} &= \mathbf{x}_i^n + \Delta t \mathbf{v}_{\|i}^n \\ &+ \sum_{j,k} \Delta x \Delta y S(\mathbf{X}_{jk} - \tilde{\mathbf{x}}_i^{n+\alpha})(1-\alpha) \left[\frac{\Delta t}{B^2} \mathbf{E}_{jk}^n \times \mathbf{B} + \frac{q_i \Delta t^2}{2m_i} \mathbf{E}_{\|jk}^n \right] . \qquad (12)\end{aligned}$$

Then, we obtain the implicit Poisson's equation in the two-dimensional system:

$$\begin{aligned}-\nabla^2 \phi_{jk}^{n+1} &- \nabla_\perp \cdot \frac{1}{\epsilon_0 B^2} \sum_i m_i S(\mathbf{X}_{jk} - \tilde{\mathbf{x}}_i^{n+1}) \nabla_\perp \phi_{jk}^{n+1} \\ &= \rho_{jk}(\tilde{\mathbf{x}}_i^{n+1})/\epsilon_0 + \delta\rho_{jk}(\tilde{\mathbf{x}}_i^{n+1})/\epsilon_0 - \delta P_{jk}(\tilde{\mathbf{x}}_i^{n+1}) , \qquad (13)\end{aligned}$$

with

$$\delta\rho_{jk}(\tilde{\mathbf{x}}_i^{n+1}) = -\nabla \cdot \sum_i q_i \delta\mathbf{x}_i S(\mathbf{X}_{jk} - \tilde{\mathbf{x}}_i^{n+1}) , \qquad (14)$$

$$\delta P_{jk}(\tilde{\mathbf{x}}_i^{n+1}) = -\nabla_\perp \cdot \left[\frac{\nabla_\perp \phi_{jk}^{n+1}}{\epsilon_0 B^2} \left(-\nabla \cdot \sum_i m_i \delta\mathbf{x}_i S(\mathbf{X}_{jk} - \tilde{\mathbf{x}}_i^{n+1}) \right) \right] . \qquad (15)$$

The displacement vector $\delta\mathbf{x}_i$ for each particle is given by

$$\delta\mathbf{x}_i = \sum_{l,m} \Delta x \Delta y S(\mathbf{X}_{lm} - \tilde{\mathbf{x}}_i^{n+1}) \alpha \left[\Delta t \frac{-\nabla \phi_{lm}^{n+1} \times \mathbf{B}}{B^2} - \frac{q_i \Delta t^2}{2m_i} \nabla_\| \phi_{lm}^{n+1} \right] . \qquad (16)$$

Solving Eqs.(9) and (10) with (13), we obtain the particle positions and velocities at the $(n+1)$-th time step.

3 Linear Properties of Simulation Scheme

3.1 Linear Analysis of Numerical Stability

In this section, we will investigate the numerical stability of our simulation scheme. According to the linear analysis given by Langdon [6], we will derive a dispersion relation in the model plasma for the one-dimensional case. Here, electron motions with respect to the background immobile ions are considered, because we are interested in stability against the plasma oscillation. Suppose a particle with an unperturbed trajectory of $x_{(0)}^{n+1} = x_{(0)}^{0} + (n+1)\Delta t v_{(0)}$ is accelerated by a sinusoidal electric field $Ee^{ikX_j - i\omega(n+1)\Delta t}$. The perturbed particle position $x_{(1)}^{n+1}$ is expressed by the time integration of acceleration in the past, such as

$$x_{(1)}^{n+1} = \frac{q\Delta t^2}{m} \sum_{s=1} \left\{ \left(s - \frac{1}{2}\right) \Delta x E \left[\alpha e^{-i\omega\Delta t} + (1-\alpha)\right] e^{-i\omega(n+1-s)\Delta t} \sum_j e^{ikX_j} S(X_j - x_{(0)}^{n+1-s+\alpha}) \right\} , \tag{17}$$

where s is a positive integer. The first term in the square bracket at $s = 1$ corresponds to the implicit acceleration by E_j^{n+1}. Since the particle feels the electric field on its unperturbed trajectory in the linear regime, the argument of the shape function becomes $X_j - x_{(0)}^{n+1-s+\alpha}$. Taking an average for all particles and operating the Fourier transformation, we obtain the dipole density $\mathcal{P}(k, n+1)$, which is separated into two parts:

$$\mathcal{P}(k, n+1) = -i\left[\mathcal{Q}(k) + \mathcal{R}(k)\right] \phi(k) e^{-i\omega(n+1)\Delta t} \tag{18}$$

where

$$\begin{aligned} \mathcal{Q}(k) &= \omega_p^2 \Delta t^2 \kappa_E(k) S(k) \\ &\quad \times \left\{ \sum_{s=2} \left(s - \frac{1}{2}\right) \left[\alpha e^{-i\omega\Delta t} + (1-\alpha)\right] e^{is\omega\Delta t} e^{-[k(s-\alpha)\Delta t]^2 v_t^2/2} \right. \\ &\quad \left. + \frac{1}{2}(1-\alpha)\, e^{i\omega\Delta t} e^{-[k(1-\alpha)\Delta t]^2 v_t^2/2} \right\} \end{aligned} \tag{19}$$

$$\mathcal{R}(k) = \omega_p^2 \Delta t^2 \kappa_E(k) S(k) \frac{1}{2} \alpha e^{-[k(1-\alpha)\Delta t]^2 v_t^2/2} . \tag{20}$$

In the above equations, we have assumed the Maxwellian velocity distribution function, $f_0(v) = (1/\sqrt{2\pi} v_t) \exp(-v^2/2v_t^2)$. Moreover, $\kappa_E(k)$ means the finite difference gradient

operator for calculating the electric field. It is worthwhile to note that the implicit term $\mathcal{R}(k)$ represents a plasma response to the electric field E^{n+1}, and that a divergence of $-\mathcal{P}(k,n+1)$ gives the charge density ρ^{n+1}/ϵ_0. Substituting the divergence of Eq.(18) into the Fourier transformation of Eq.(4), we arrive at the dispersion relation of the implicit particle simulation plasma,

$$1+\frac{1}{K^2(k)}\sum_p S(k_p)\left[k_p\mathcal{Q}(k_p)+\kappa_{\delta\rho}(k)\mathcal{R}(k_p)\right]=0\ , \tag{21}$$

where $\kappa_{\delta\rho}(k)$ is the divergence operator for the implicit term in Eq.(7) and $K^2(k)$ means the Laplacian in the finite difference form. The index p shows the alias mode which arises in the calculation of the charge density defined on the spatial grids. Then, k_p is given by $k_p=k-p(2\pi/\Delta x)$. If the alias modes can be ignored, and if $\kappa_{\delta\rho}(k)=k$, we can simplify the dispersion relation of Eq.(21) as follows,

$$\begin{aligned}&1+\frac{\omega_p^2\Delta t^2}{K^2(k)}k\kappa_E(k)S^2(k)\\ &\quad\times\ \sum_{s=1}\left(s-\frac{1}{2}\right)\left[\alpha e^{-i\omega\Delta t}+(1-\alpha)\right]e^{is\omega\Delta t}e^{-[k(s-\alpha)\Delta t]^2v_t^2/2}=0\ .\end{aligned} \tag{22}$$

In remainder of this section, we numerically solve Eqs.(21) and (22) in a frequency domain of the plasma oscillation, and examine the numerical stability of our simulation method.

Firstly, let us consider a case without the aliasing effect ($p=0$), calculating real and imaginary parts of ω (i.e., ω_r and ω_i) in Eq.(22) by the Newton method. In our actual simulation code, we have used the following operators:

$$K^2(k) = k^2\left[\frac{\sin(k\Delta x/2)}{k\Delta x/2}\right]^2 \tag{23}$$

$$\kappa_E(k) = k\left[\frac{\sin(k\Delta x)}{k\Delta x}\right] \tag{24}$$

$$\kappa_{\delta\rho}(k) = k\ . \tag{25}$$

We take the divergence of Eq.(7) in the wavenumber space so that Eq.(25) is satisfied. Hence, Eq.(22) is valid when the alias modes are dismissed. The shape function which we have employed is the *linear-interpolation* function,

$$S(k)=\left[\frac{\sin(k\Delta x/2)}{k\Delta x/2}\right]^2\ . \tag{26}$$

Numerical solutions of Eq.(22) with parameters of $\Delta x = 12.5\pi\lambda_D$ and $\alpha = 0.5$ are shown in Fig.1(a), where contours of ω_r and ω_i are plotted in $\Delta t - k$ plane. ω_r decreases as Δt and k increases, respectively, because of the implicit time-difference and the finite grid effect. The minimum frequency in the $\Delta t - k$ plane is $\omega_r = 0.147\omega_p$. More importantly, ω_i has a small negative value for $\omega_p \Delta t \gg 1$. Our implicit scheme is, thus, numerically stable, when the alias modes are ignored.

Secondly, we solve Eq.(21) under the same numerical parameters and operators as in the case of Fig.1(a). Here, the aliasing effect ($p \neq 0$) is fully taken into account. The numerical result is given in Fig.1(b). One can see that the decrement of ω_r against k is larger than that of the case shown in Fig.1(a). Undesirably, there are unstable solutions (positive ω_i) due to the aliasing effect in a wide range of the wavenumber space. The numerical instability caused by the alias modes can be stabilized, if we use a much smaller grid spacing such as $\Delta x \sim \lambda_D$. In order to realize a particle simulation with an MHD spatial scale, however, it is necessary to take a large grid spacing ($\Delta x \gg \lambda_D$). Although the employment of a higher order (much smoother) shape function is a candidate to suppress the numerical instability, it makes the simulation code much more complicated. Thus, we will introduce a stabilizing effect of the time-decentered scheme, increasing the decentering parameter α.

We have plotted solutions of Eq.(21) with $\alpha = 0.55$ in Fig.1(c). While ω_r is quite similar to the case in Fig.1(b), ω_i in $\Delta t - k$ space is largely modified by the time-decentering effect. The unstable solution, $\omega_i > 0$, is confined in a large wavenumber region, $k\Delta x > 0.3\pi$. No unstable solution is found in a small wavenumber region, $k\Delta x < 0.3\pi$, even in the case of $\omega_p \Delta t \gg 1$. If we further introduce an adequate numerical filter which can damp the large wavenumber mode of $k\Delta x > 0.3\pi$, we can realize a stable simulation code against the large time step ($\omega_p \Delta t \gg 1$) and the large grid spacing ($\Delta x \gg \lambda_D$). Therefore, we will use a numerical filter defined by the following equation [1],

$$W(k) = \exp\left[-(k/k_c)^{N_f}\right] . \tag{27}$$

Here, the cutoff wavenumber of $k_c = 2\pi/8\Delta x$ is sufficient for our purpose. The integer N_f, which is set to be 4 or 8 in the later simulations, controls the sharpness of the numerical filter. In addition, the numerical filter should be employed both for $\rho(\tilde{x}_i^{n+1})$ and $\delta\rho(\tilde{x}_i^{n+1})$ consistently, as was discussed in Ref.[3]. Otherwise, usage of the numerical filter will

degrade accuracy of the electrostatic field calculation.

3.2 Exact Treatment of the Implicit Term

In obtaining the future electrostatic potential ϕ^{n+1} in an implicit particle simulation, the implicit Poisson's equation such as Eq.(4) is employed. After having solved the implicit equation, particles are pushed by the electric field E^{n+1} $(= -\nabla\phi^{n+1})$. Hence, it is not guaranteed that the future charge density $\rho(x_i^{n+1})$ and ϕ^{n+1} satisfy the Poisson's equation, that is, Eq.(3). Before going into a real simulation, therefore, we must examine how the numerical error due to the implicit term $\delta\rho$ arises, and how large it is.

Suppose that the finite grid effects be neglected for simplicity, then the implicit term $\delta\rho(x)$ given by Eq.(7) can be expressed as follows:

$$\delta\rho_{exact}(x) = -\nabla\cdot C\int dx' n_c(x')S(x-x')\int dx'' E(x'')S(x-x'')\ , \tag{28}$$

where $n_c(x)$ is the density of the particle center. The constant C is defined as $C = \alpha q^2\Delta t^2/2m$. For the sake of comparison with the exact case of Eq.(7), we shall examine the conventional simplified form of the implicit term in Eq.(8), which is rewritten as

$$\delta\rho_{simpl.}(x) = -\nabla\cdot CE(x)\int dx' n_c(x')S(x-x')\ . \tag{29}$$

Fourier transformation of the above two equations gives

$$\delta\rho_{exact}(k) = -i\kappa_{\delta\rho}(k)C\int\frac{dk'}{2\pi}n_c(k-k')S(k)E(k')S(k') \tag{30}$$

$$\delta\rho_{simpl.}(k) = -i\kappa_{\delta\rho}(k)C\int\frac{dk'}{2\pi}n_c(k-k')S(k-k')E(k')\ . \tag{31}$$

Apparently, $\delta\rho_{exact}(k)$ and $\delta\rho_{simpl.}(k)$ exactly coincide, if $k = 0$ or $S(x)$ is the delta function. When $E(k)$ is monochromatic $(k = k')$, $\delta\rho_{exact}$ and $\delta\rho_{simpl.}$ are, respectively, given by

$$\delta\rho_{exact}(k) = -i\kappa_{\delta\rho}(k)Cn_c(0)S^2(k)E_k \tag{32}$$

$$\delta\rho_{simpl.}(k) = -i\kappa_{\delta\rho}(k)Cn_c(0)S(0)E_k\ . \tag{33}$$

For a finite value of k and for the shape function $S(k)$ defined by Eq.(26), thus, the approximation used in Eq.(8) causes a difference between $\delta\rho_{exact}$ and $\delta\rho_{simpl.}$. In large

wavenumber regime, especially. $\delta\rho_{simpl}$ is independent of $S(k)$, while $\rho^{n+1}(k)$ is proportional to $S^2(k)$. Hence, it is expected from Eqs.(4) and (33) that the electrostatic potential obtained under the approximation of Eq.(8) is under-estimated when $k \neq 0$.

Furthermore, in order to solve Eq.(4) directly, we shall move the implicit term to the left hand side. Then, Eq.(4) is rewritten in a matrix form,

$$M_{jk}\phi_k^{n+1} = \rho_j(\tilde{x}_i^{n+1}) \ . \tag{34}$$

When the implicit Poisson's equation is solved in the real space, it is difficult to operate the numerical filter on the implicit term. This is because the filter should be transformed into the real space in terms of a convolution operator which will, generally, lead to a large number of non-zero elements of M_{jk}. Thus, the numerical filter does not operate on the implicit term moved into the left hand side, and hence, the treatment of the implicit term is inconsistent with the filtering of the charge density $\rho(\tilde{x}_i^{n+1})$. In addition to the simplification of the implicit term, the inconsistent filtering enhances the error in the electrostatic field calculation. The numerical accuracy of the electrostatic field is estimated in the linear regime by

$$\delta \equiv \frac{\epsilon_0 K^2(k)\phi^{n+1}(k)}{\rho^{n+1}(k)} \approx \frac{1}{1+(\alpha/2)\omega_p^2\Delta t^2(1-S^2(k)W^2(k))} \ . \tag{35}$$

Here, the Fourier transformation of the finite difference operators are approximated by the wavenumber k. Through the actual one-dimensional simulation in the next section, we examine the value of δ both for the cases with the exact (Eq.(7)) and simplified (Eq.(8)) implicit terms.

4 Simulation Results

4.1 Numerical Accuracy in Electrostatic Field Calculation

Giving an initial density perturbation of $\delta n \propto \sin(kx)$ for both the electrons and ions, we have performed several one-dimensional simulations for varying wavenumbers over hundred time steps with the periodic boundary condition. Parameters used in the simulations are as follows: $\alpha = 0.55$, $L_x = 128\Delta x$, $\Delta x = 12.5\pi\lambda_D$, $\Delta t = 10\omega_p^{-1}$, $m_i = 100m_e$, and $T_i = 0.01T_e$, where L_x means the system length; m_i, m_e, T_i and T_e denote the

masses and the temperatures of the ions and electrons. We have employed 1,024 particles per grid spacing both for the electrons and ions. Averaged value of δ over a hundred time steps is plotted as a function of the wavenumber in Fig.2, where the white and black circles, respectively, represent the results for the cases with the exact and simplified implicit terms. Dashed line indicates the analytical estimation given by Eq.(35). In the case of the exact implicit term, the value of δ are irrespective of k and nearly equal to 1. The numerical error is less than 5%. Employing the exact expression of the implicit term in Eq.(7), therefore, we can perform a simulation run with high numerical accuracy for the potential calculation. In the simplified case, however, the value of δ monotonously decreases as k increases, as the analytical prediction, i.e., Eq.(35), gives. Large difference between $\epsilon_0 K^2(k)\phi^{n+1}(k)$ and $\rho^{n+1}(k)$ arises for a much smaller wavenumber regime than the cutoff wavenumber k_c $(= 2\pi/8\Delta x)$, for example, the error reaches to 60% of $\rho^{n+1}(k)$ at $k = 6\pi/64\Delta x$.

4.2 Dispersion Relation of Electrostatic Waves

Employing the exact implicit term given in Eq.(7), we have performed the simulation runs for the same parameters with those in the last subsection. In the present simulations, 8,192 particles per grid spacing are used. We have obtained the dispersion relation of the electrostatic waves after having run the simulation code over 8,192 time steps. Throughout the simulation run, the total energy in the simulation system is conserved within an error of 1%.

The power spectra of the electrostatic potential in the ω-k plane are plotted in Fig.3. The dashed curve represents the dispersion relation of the ion acoustic wave, that is, $\omega = kC_s$ $(C_s = \sqrt{T_e/m_i})$. In low frequency regime ($\omega \sim 10^{-4}$-$10^{-3}\omega_p$), one can find the significant peaks which are coincident with the theoretical dispersion relation of the ion acoustic mode. The plasma oscillation, of which the frequency ($\omega_{pm} \simeq 0.27\omega_p$) is modulated by the implicit time-difference, can also be detected in the power spectra. The observed frequencies for the above two modes are in good agreement with the theoretical values.

In the power spectra, we have found two artificial modes. One of them, which may be generated by the numerical error in Eq.(4), is seen at the Nyquist frequency $\omega_N = \pi/\Delta t$.

The other mode in an intermediate frequency range of $\omega \sim 10^{-2}$-$10^{-1}\omega_p$ would be caused by the mode coupling of ω_{pm} and ω_N. This is because the frequency spectra with band width of $0.06\omega_p$ are centered around $\omega_N - \omega_{pm}$ and the band width is similar to that of the frequency-modulated plasma oscillation. Moreover, we have confirmed that the power spectra of the artificial modes are independent of the ion to electron mass ratio. The artificial modes, thus, will not affect the low-frequency wave dynamics where the dynamics of ions plays the leading role.

4.3 Simulation of the ITG Drift Instability

We have performed two-dimensional simulations of the ITG drift instability in a system with a shearless slab geometry for several different time steps. The simulation system is set in the x-y plane. External magnetic field in the y-z plane is imposed on the system with an inclination angle of $\theta = \tan^{-1}(k_\parallel/k_\perp)$, where $\theta = 0.01$ in the present simulations. The electrostatic potential is fixed to zero at $x = 0$ and L_x, while the periodic boundary condition is employed in the y direction. The ion temperature profile in the x direction is given by

$$T_i(x) = T_{i0}\kappa_T L_x \frac{\exp(-\kappa_T x)}{1 - \exp(-\kappa_T L_x)} , \tag{36}$$

where $\kappa_T = 1.6 \times 10^{-3}\lambda_D^{-1}$ and $T_{i0} = T_e$. Other parameters are set as follows; the system length $L_x = L_y = 16\Delta$, the grid spacing $\Delta = \Delta x = \Delta y$, the ion to electron mass ratio $m_i/m_e = 1836$, and number of particles per unit cell $N\Delta = 1024$. The magnetic field intensity is determined so that $\Omega_e = \omega_p$, where Ω_e is the electron cyclotron frequency. In the two-dimensional case with the inclined magnetic field and the polarization term, the critical time step Δt_c for the explicit time integration is governed by the electrostatic shear Alfvén frequency [7] $\omega_H = (k_\parallel/k_\perp)(m_e/m_i)^{1/2}\Omega_e$; i.e., $\Delta t_c = \omega_H^{-1} = 4285\omega_p^{-1}$ for the present parameters. Thus, we will show that our implicit scheme is numerically stable for the time step Δt larger than Δt_c, while the explicit scheme is unstable in the case of $\Delta t > \Delta t_c$. We have carried out five simulation runs, changing the time step ($\Delta t = 2.5 \times 10^3$-$3 \times 10^4\omega_p^{-1}$). In the following simulations, only the ITG mode with wavelength of L_y can be excited, because shorter wavelength modes ($k \geq k_c = 2\pi/8\Delta$) are artificially damped by the numerical filter for stabilization of the scheme.

Time evolution of the electric field energy is shown in Fig.4. Here, $\Delta = 62.5\pi\lambda_D$

and $\Delta t = 1 \times 10^4 \omega_p^{-1}$. The field energy exponentially increases with the growth rate of $4.0 \times 10^{-7} \omega_p$ as the ITG drift instability is generated. Using the maximum entropy method, we have calculated the real frequency to obtain $\omega_r = 6 \times 10^{-7} \omega_p$. The frequency and growth rate obtained from the simulation are fairly in good agreement with the theoretical estimate given by the well-known dispersion relation under the fluid approximation [8]

$$\omega = \left(\frac{1}{2} + i \frac{\sqrt{3}}{2} \right) \left(\frac{k_\parallel^2 C_s^2}{2} \omega_{Ti}^* \right)^{1/3} . \tag{37}$$

For the present parameters, $\omega = 3.5 \times 10^{-7} + i 6.0 \times 10^{-7} \omega_p$. The instability saturates at $t = 2.2 \times 10^7 \omega_p^{-1}$. The saturation level of the field energy is about $10^{-7} n T_e$. In Table I, the growth rates of the instability are summarized for the cases of $\Delta t = 0.25$, 0.5, 1.0, 2.0, and $3.0 \times 10^4 \omega_p^{-1}$. As is seen in Table I, the growth rate fluctuates in the large Δt regime owing to the numerical error. Nonetheless, all saturation levels of the field energy for the five cases are nearly equal to $10^{-7} n T_e$. Therefore, our implicit scheme is said to be stable even if $\Delta t > \Delta t_c$, and is applicable to a real low frequency phenomenon such as the ITG drift instability.

5 Summary and Discussion

In the present study, we have developed an advanced electrostatic version of the macro-scale implicit particle simulation code (AMACS-ES), and have examined its characteristics analytically and numerically. The results are summarized as follows.

1. We have derived the linear dispersion relation of our new implicit particle simulation algorithm, and have verified its stability by solving the dispersion relation numerically. The linear analysis has shown that the unstable solutions due to the aliasing effect exist in the wide wavenumber regime for the time-centered difference scheme. In order to suppress the numerical instability, we have introduced the stabilizing effect of the time-decentered scheme, and have employed the numerical filter leading to the damping of large wavenumber modes.

2. The numerical method for solving the implicit Poisson's equation has been greatly improved in this study. The exact implicit term is employed instead of the simplified form. The accuracy of the electrostatic field calculation, thus, becomes much improved. The

improvement is verified by the actual simulations. We have also revealed the dangerous degradation of the numerical accuracy for the simplified implicit term and the inconsistent filtering.

3. The dispersion relations of electrostatic waves have been examined by means of the one-dimensional simulation. The power spectra in the ω-k space have shown good coincidence with the theoretical dispersion relation. Especially, the ion acoustic branch is clearly identified in the ω-k diagram.

4. Based on the scheme developed in one-dimensional case, we have extended our code to the two-dimensional geometry with the external magnetic field. In the two-dimensional model, the effect of the polarization drift is taken into account. Giving the ion temperature gradient perpendicular to the magnetic field, we have carried out simulations of the ITG drift instability. The obtained frequency and growth rate of the most unstable ITG mode are in reasonably good agreement with theoretically predicted ones. The growth rate of the instability, however, is found to fluctuate in a certain range when the time step Δt is changed as shown in Table I.

For stabilization of the alias modes, the high-frequency waves, such as the plasma oscillation in the one-dimensional case and the electrostatic shear Alfvén wave in the two-dimensional case, are artificially attenuated in our scheme. Strictly speaking, the total energy in the implicit particle simulation plasma is not conserved, since the artificial damping of plasma waves causes numerical cooling of particles. For example, the total energy in the simulation of $\Delta t = 1.0 \times 10^4 \omega_p^{-1}$ in section 4.3 fluctuates within a level of 0.01% of the initial value. The energy conservation rate observed in the simulation is not sufficient for our purpose, when we intend to simulate a weakly-saturated instability such as the ITG drift instability. This is because the loss of the kinetic energy ($\sim 3.0 \times 10^{-4} nT_e$ at the end of the simulation) is not completely compensated by the increase of the field energy ($\sim 1.3 \times 10^{-7} nT_e$) and the ion sloshing energy [7] ($\sim 2.4 \times 10^{-4} nT_e$). In this case, 20% of the decrement of the kinetic energy is lost because of the numerical cooling, which may result in the fluctuation of the growth rate seen in Table I. In order to reduce the excessive cooling, it is important to suppress the numerical noise associated with the high-frequency waves. The δf method [9] is one potential candidate which can decrease the numerical noise resulting from the finite number of particles. Since the δf method

is designed for an explicit time integration, however, we need to develop an implicit δf method.

Acknowledgments

Numerical computations in this study are performed on the NIFS Advanced Computing System for Complexity Simulation. This work is partially supported by Grants-in-Aid of the Minstry of Education, Science and Culture (No.05836038 and No.06044238).

References

1. C.K. Birdsall and A.B. Langdon, *Plasma Physics via Computer Simulation* (McGraw Hill, New York, 1985).

2. T. Tajima, *Computational Plasma Physics: With Applications to Fusion and Astrophysics* (Addison-Wesly, New York, 1989).

3. A.B. Langdon, B.I. Cohen, and A. Friedman, *J. Compu. Phys.*, **51**, 107 (1983).

4. D.C. Barnes, T. Kamimura, J.-N. Leboeuf, and T. Tajima, *J. Compu. Phys.*, **52**, 480 (1983)

5. M. Tanaka, *J. Compu. Phys.*, **79**, 209 (1988).

6. A.B. Langdon, *J. Compu. Phys.*, **30**, 202 (1979).

7. W.W. Lee, *J. Compu. Phys.*, **72**, 243 (1987).

8. L.I. Rudakov and R.Z. Sagdeev, *Sov. Phys.-Dokl.*, **6**, 415 (1961).

9. S.E. Parker and W.W. Lee, *Phys. Fluids*, **B5**, 77 (1993).

TABLE I

Growth rates of the ITG drift instability for different time steps.

Time Step (ω_p^{-1})	Growth Rate (ω_p)
2.5×10^3	4.9×10^{-7}
5.0×10^3	4.9×10^{-7}
1.0×10^4	4.0×10^{-7}
2.0×10^4	2.8×10^{-7}
3.0×10^4	3.9×10^{-7}

Figure Captions

FIG. 1. Numerical solutions of the dispersion relation obtained from the linear analysis of the simulation scheme for the cases of (a) $\alpha = 0.5$ without the alias modes, (b) $\alpha = 0.5$ and (c) $\alpha = 0.55$ with the alias modes. Solid and dashed contour lines indicate positive and negative values, respectively. For the real part of the solutions (left), the contour interval of ω_r/ω_p is 0.1 in all cases of (a)-(c). For the imaginary part (right), the contour levels in case (a) are logarithmically defined as -10^{-10}, -10^{-9}, ... , and -10^{-4}; in cases (b) and (c), the contour interval of ω_i/ω_p is equal to 4×10^{-3}.

FIG. 2. Plots of the electrostatic fields obtained from the actual simulation runs with the exact (white circles) and simplified (black circles) implicit terms. Dashed line shows the theoretical estimation given by Eq.(35) where both the simplification of the implicit term and the inconsistent filtering are employed.

FIG. 3. Power spectra of the electrostatic potential obtained from the one-dimensional simulation. Dashed curve represents the theoretical dispersion relation of the ion acoustic mode.

FIG. 4. Time evolution of the electric field energy for the two-dimensional simulation of the ITG drift instability. In this case, the simulation time step is set to be $1 \times 10^4 \omega_p^{-1}$. The growth rate of the instability obtained by the simulation is consistent with the theoretical value based on the fluid approximation.

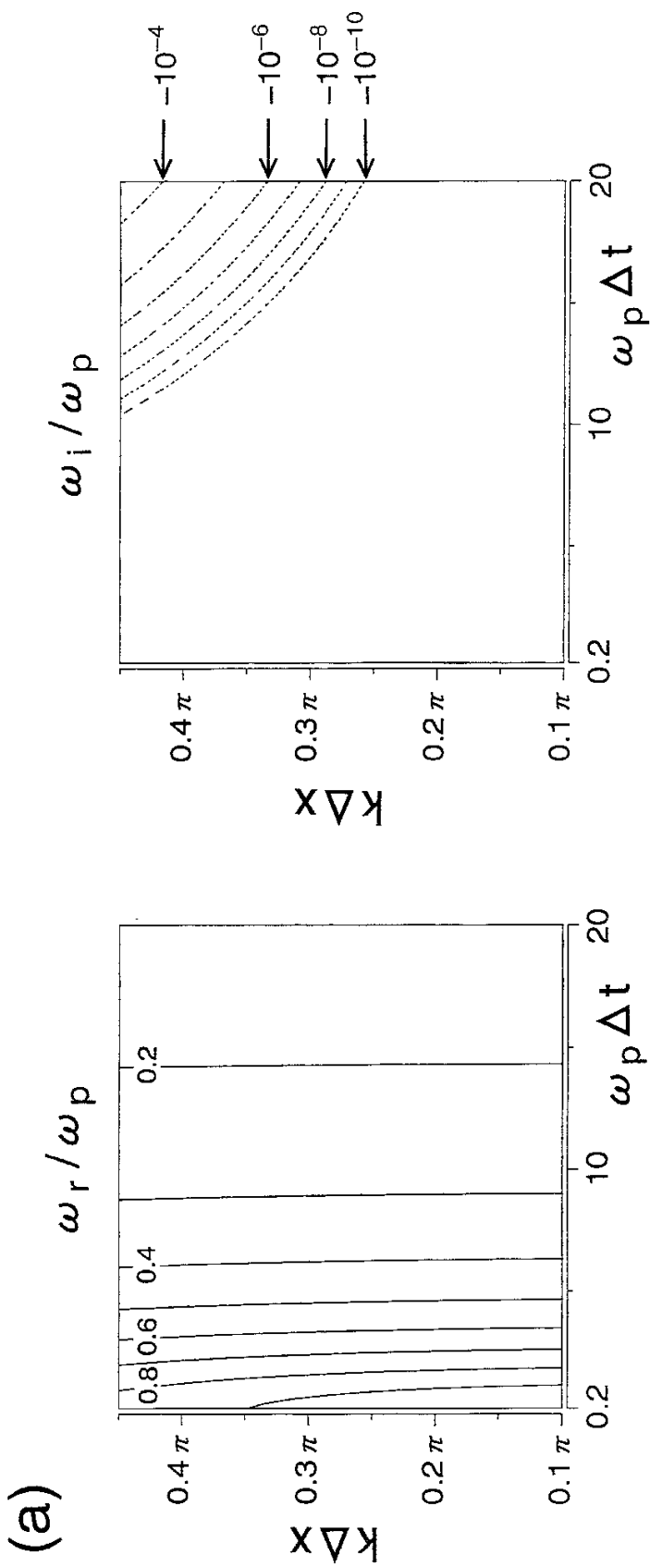
(a)
ω_r / ω_p
0.8
0.6
0.4
0.2
$k\Delta x$
0.4 π
0.3 π
0.2 π
0.1 π
0.2
10
20
$\omega_p \Delta t$
ω_i / ω_p
-10^{-4}
-10^{-6}
-10^{-8}
-10^{-10}

Figure 1(a)

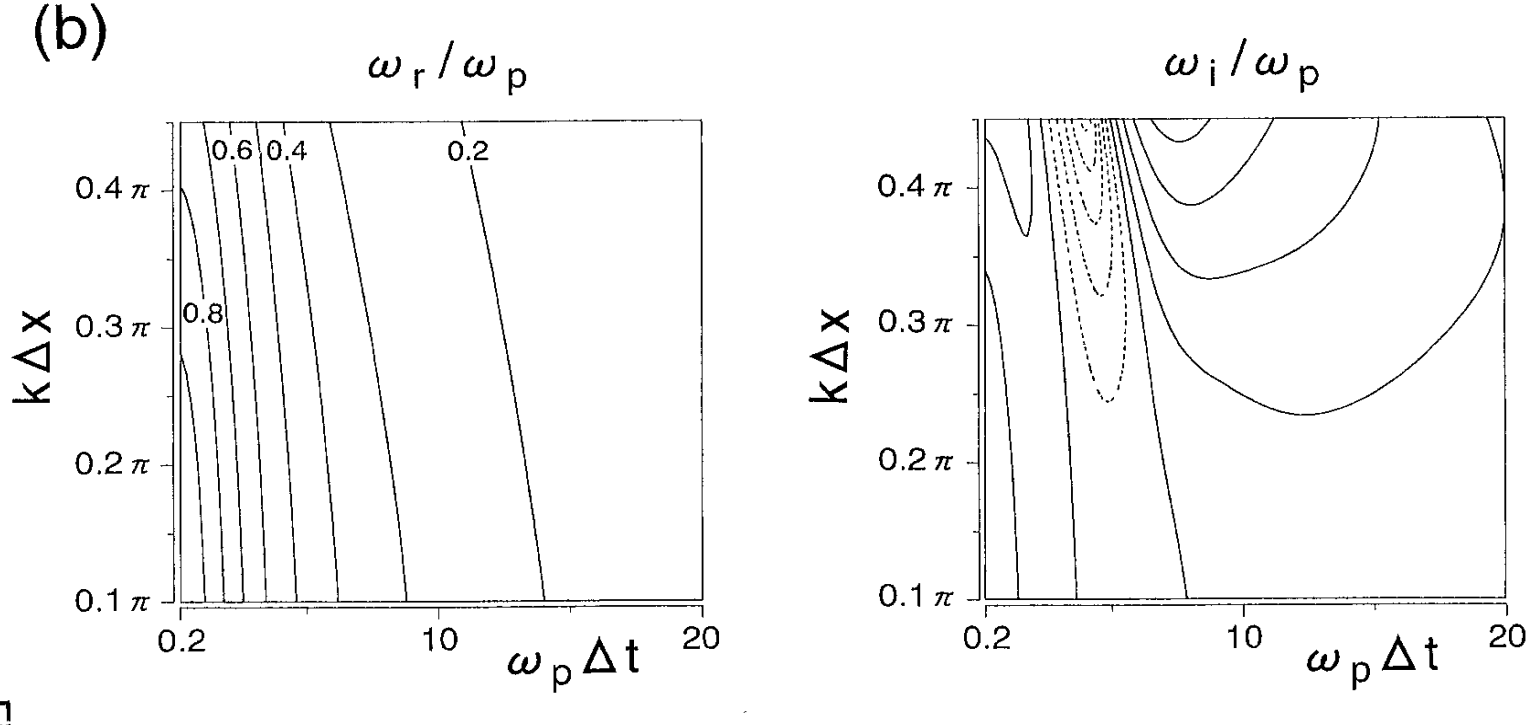
(b)
ω_r / ω_p
ω_i / ω_p
0.6
0.4
0.2
0.8
$k\Delta x$
0.4 π
0.3 π
0.2 π
0.1 π
0.2
10
20
$\omega_p \Delta t$

Figure 1(b)

(c)
ω_r / ω_p
0.2
0.4
0.6
0.8
$k\Delta x$
0.4 π
0.3 π
0.2 π
0.1 π
0.2
10
20
$\omega_p \Delta t$
ω_i / ω_p
$k\Delta x$
0.4 π
0.3 π
0.2 π
0.1 π
0.2
10
20
$\omega_p \Delta t$

Figure 1(c)

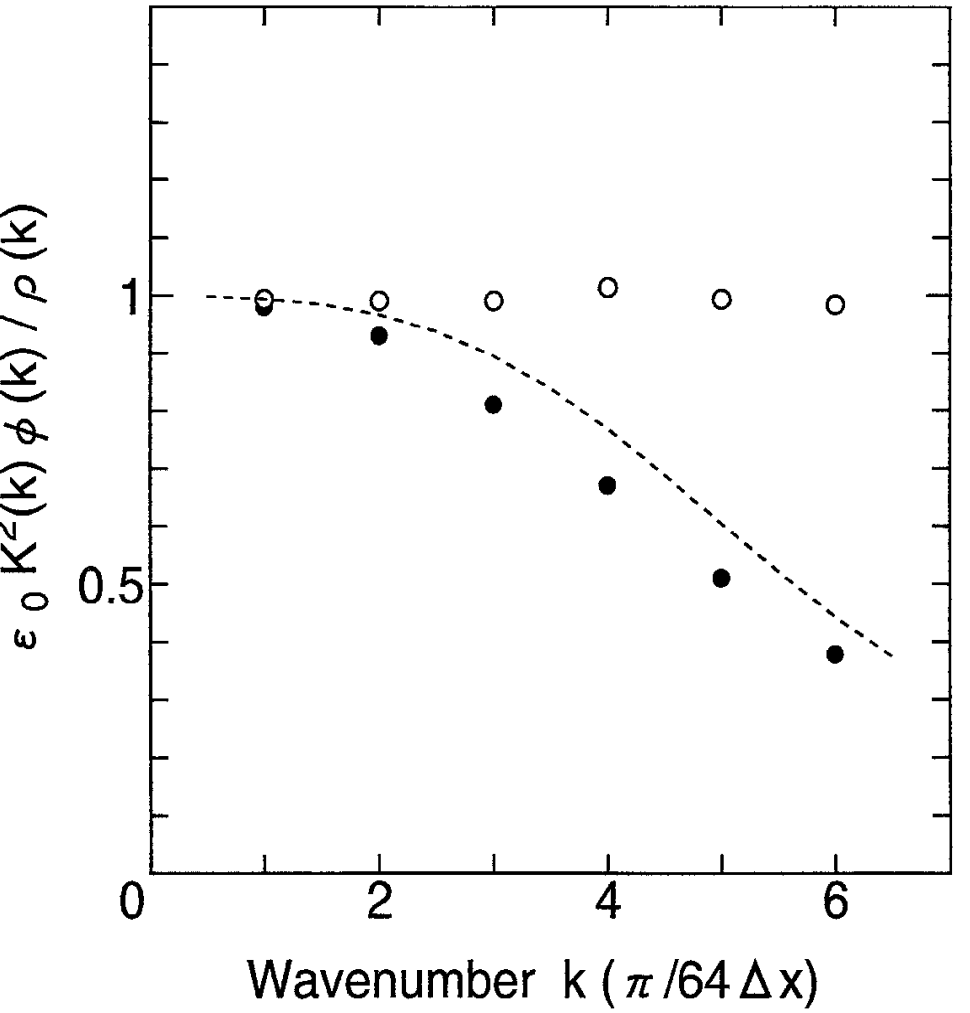
$\varepsilon_0 K^2(k) \phi(k) / \rho(k)$
1
0.5
0
2
4
6
Wavenumber k (π /64 Δ x)

Figure 2

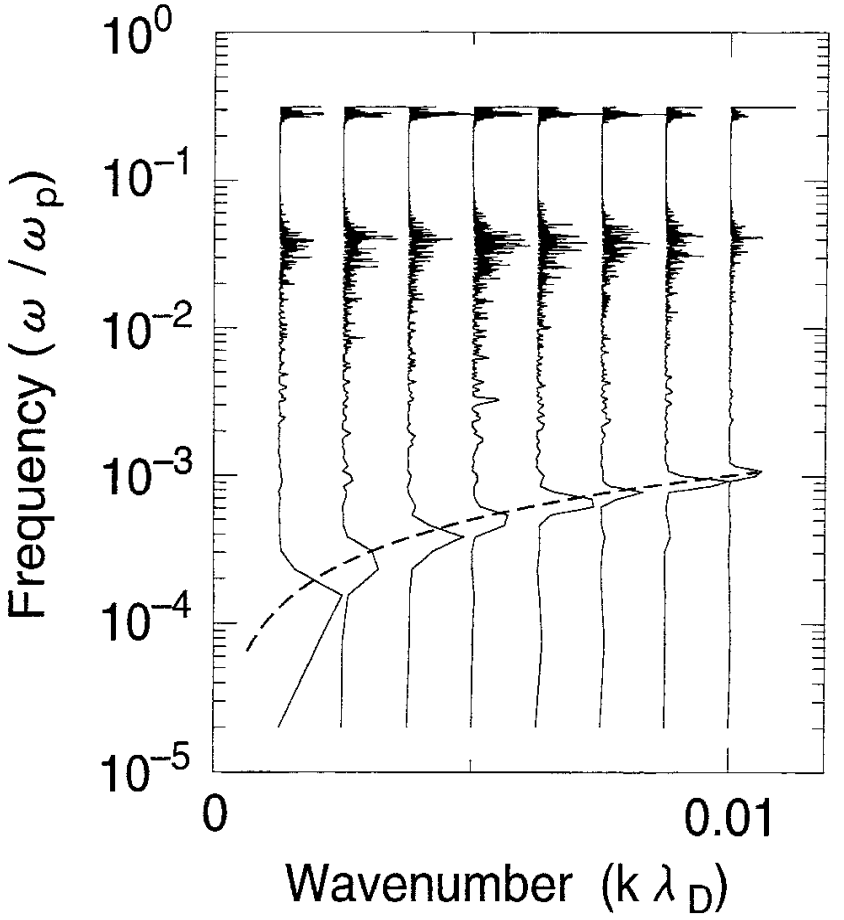
10^0
10^{-1}
10^{-2}
10^{-3}
10^{-4}
10^{-5}
Frequency (ω / ω_p)
0
0.01
Wavenumber (k λ_D)

Figure 3

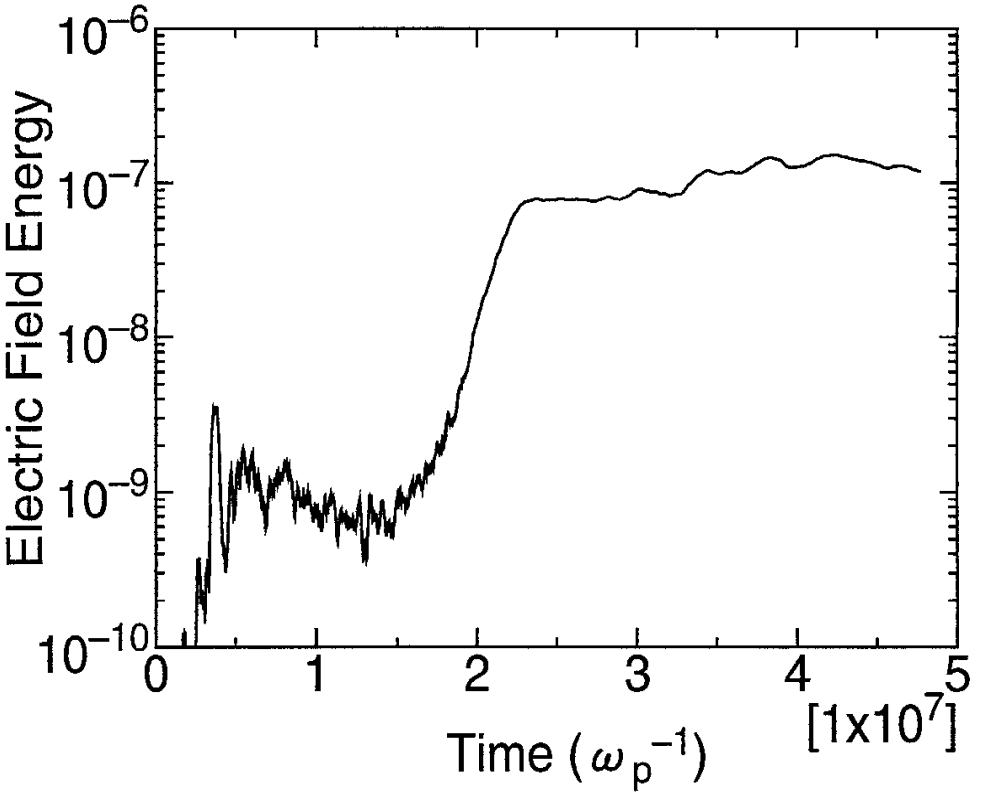
Electric Field Energy
10^{-6}
10^{-7}
10^{-8}
10^{-9}
10^{-10}
0
1
2
3
4
5
[1x10^{7}]
Time (ω_p^{-1})

Figure 4

Recent Issues of NIFS Series

NIFS-291 H. Idei, K. Ida, H. Sanuki, S. Kubo, H. Yamada, H. Iguchi, S. Morita, S. Okamura, R. Akiyama, H. Arimoto, K. Matsuoka, K. Nishimura, K. Ohkubo, C. Takahashi, Y. Takita, K. Toi, K. Tsumori and I. Yamada, *Formation of Positive Radial Electric Field by Electron Cyclotron Heating in Compact Helical System*; July 1994

NIFS-292 N. Noda, A. Sagara, H. Yamada, Y. Kubota, N. Inoue, K. Akaishi, O. Motojima, K. Iwamoto, M. Hashiba, I. Fujita, T. Hino, T. Yamashina, K. Okazaki, J. Rice, M. Yamage, H. Toyoda and H. Sugai, *Boronization Study for Application to Large Helical Device*; July 1994

NIFS-293 Y. Ueda, T. Tanabe, V. Philipps, L. Könen, A. Pospieszczyk, U. Samm, B. Schweer, B. Unterberg, M. Wada, N. Hawkes and N. Noda, *Effects of Impurities Released from High Z Test Limiter on Plasma Performance in TEXTOR*; July. 1994

NIFS-294 K. Akaishi, Y. Kubota, K. Ezaki and O. Motojima, *Experimental Study on Scaling Law of Outgassing Rate with A Pumping Parameter*, Aug. 1994

NIFS-295 S. Bazdenkov, T. Sato, R. Horiuchi, K. Watanabe, *Magnetic Mirror Effect as a Trigger of Collisionless Magnetic Reconnection*, Aug. 1994

NIFS-296 K. Itoh, M. Yagi, S.-I. Itoh, A. Fukuyama, H. Sanuki, M. Azumi, *Anomalous Transport Theory for Toroidal Helical Plasmas*, Aug. 1994 (IAEA-CN-60/D-III-3)

NIFS-297 J. Yamamoto, O. Motojima, T. Mito, K. Takahata, N. Yanagi, S. Yamada, H. Chikaraishi, S. Imagawa, A. Iwamoto, H. Kaneko, A. Nishimura, S. Satoh, T. Satow, H. Tamura, S. Yamaguchi, K. Yamazaki, M. Fujiwara, A. Iiyoshi and LHD group, *New Evaluation Method of Superconductor Characteristics for Realizing the Large Helical Device;* Aug. 1994 (IAEA-CN-60/F-P-3)

NIFS-298 A. Komori, N. Ohyabu, T. Watanabe, H. Suzuki, A. Sagara, N. Noda, K. Akaishi, N. Inoue, Y. Kubota, O Motojima, M. Fujiwara and A. Iiyoshi, *Local Island Divertor Concept for LHD*; Aug. 1994 (IAEA-CN-60/F-P-4)

NIFS-299 K. Toi, T. Morisaki, S. Sakakibara, A. Ejiri, H. Yamada, S. Morita, K. Tanaka, N. Nakajima, S. Okamura, H. Iguchi, K. Ida, K. Tsumori, S. Ohdachi, K. Nishimura, K. Matsuoka, J. Xu, I. Yamada, T. Minami, K. Narihara, R. Akiyama, A. Ando, H. Arimoto, A. Fujisawa, M. Fujiwara, H. Idei, O. Kaneko, K. Kawahata, A. Komori, S. Kubo, R. Kumazawa, T. Ozaki, A. Sagara, C. Takahashi, Y. Takita and T. Watari, *Impact of Rotational-Transform Profile Control on Plasma Confinement and Stability in CHS*; Aug. 1994 (IAEA-CN-60/A6/C-P-3)

NIFS-300 H. Sugama and W. Horton,
Dynamical Model of Pressure-Gradient-Driven Turbulence and Shear Flow Generation in L-H Transition; Aug. 1994 (IAEA/CN-60/D-P-I-11)

NIFS-301 Y. Hamada, A. Nishizawa, Y. Kawasumi, K.N. Sato, H. Sakakita, R. Liang, K. Kawahata, A. Ejiri, K. Narihara, K. Sato, T. Seki, K. Toi, K. Itoh, H. Iguchi, A. Fujisawa, K. Adachi, S. Hidekuma, S. Hirokura, K. Ida, M. Kojima, J. Koog, R. Kumazawa, H. Kuramoto, T. Minami, I. Negi, S. Ohdachi, M. Sasao, T. Tsuzuki, J. Xu, I. Yamada, T. Watari,
Study of Turbulence and Plasma Potential in JIPP T-IIU Tokamak; Aug. 1994 (IAEA/CN-60/A-2-III-5)

NIFS-302 K. Nishimura, R. Kumazawa, T. Mutoh, T. Watari, T. Seki, A. Ando, S. Masuda, F. Shinpo, S. Murakami, S. Okamura, H. Yamada, K. Matsuoka, S. Morita, T. Ozaki, K. Ida, H. Iguchi, I. Yamada, A. Ejiri, H. Idei, S. Muto, K. Tanaka, J. Xu, R. Akiyama, H. Arimoto, M. Isobe, M. Iwase, O. Kaneko, S. Kubo, T. Kawamoto, A. Lazaros, T. Morisaki, S. Sakakibara, Y. Takita, C. Takahashi and K. Tsumori,
ICRF Heating in CHS; Sep. 1994 (IAEA-CN-60/A-6-I-4)

NIFS-303 S. Okamura, K. Matsuoka, K. Nishimura, K. Tsumori, R. Akiyama, S. Sakakibara, H. Yamada, S. Morita, T. Morisaki, N. Nakajima, K. Tanaka, J. Xu, K. Ida, H. Iguchi, A. Lazaros, T. Ozaki, H. Arimoto, A. Ejiri, M. Fujiwara, H. Idei, A. Iiyoshi, O, Kaneko, K. Kawahata, T. Kawamoto, S. Kubo, T. Kuroda, O. Motojima, V.D. Pustovitov, A. Sagara, C. Takahashi, K. Toi and I. Yamada,
High Beta Experiments in CHS; Sep. 1994 (IAEA-CN-60/A-2-IV-3)

NIFS-304 K. Ida, H. Idei, H. Sanuki, K. Itoh, J. Xu, S. Hidekuma, K. Kondo, A. Sahara, H. Zushi, S.-I. Itoh, A. Fukuyama, K. Adati, R. Akiyama, S. Bessho, A. Ejiri, A. Fujisawa, M. Fujiwara, Y. Hamada, S. Hirokura, H. Iguchi, O. Kaneko, K. Kawahata, Y. Kawasumi, M. Kojima, S. Kubo, H. Kuramoto, A. Lazaros, R. Liang, K. Matsuoka, T. Minami, T. Mizuuchi, T. Morisaki, S. Morita, K. Nagasaki, K. Narihara, K. Nishimura, A. Nishizawa, T. Obiki, H. Okada, S. Okamura, T. Ozaki, S. Sakakibara, H. Sakakita, A. Sagara, F. Sano, M. Sasao, K. Sato, K.N. Sato, T. Saeki, S. Sudo, C. Takahashi, K. Tanaka, K. Tsumori, H.Yamada, I. Yamada, Y. Takita, T. Tuzuki, K. Toi and T. Watari,
Control of Radial Electric Field in Torus Plasma; Sep. 1994 (IAEA-CN-60/A-2-IV-2)

NIFS-305 T. Hayashi, T. Sato, N. Nakajima, K. Ichiguchi, P. Merkel, J. Nührenberg, U. Schwenn, H. Gardner, A. Bhattacharjee and C.C.Hegna,
Behavior of Magnetic Islands in 3D MHD Equilibria of Helical Devices; Sep. 1994 (IAEA-CN-60/D-2-II-4)

NIFS-306 S. Murakami, M. Okamoto, N. Nakajima, K.Y. Watanabe, T. Watari, T. Mutoh, R. Kumazawa and T. Seki,

Monte Carlo Simulation for ICRF Heating in Heliotron/Torsatrons; Sep. 1994 (IAEA-CN-60/D-P-I-14)

NIFS-307 Y. Takeiri, A. Ando, O. Kaneko, Y. Oka, K. Tsumori, R. Akiyama, E. Asano, T. Kawamoto, T. Kuroda, M. Tanaka and H. Kawakami,
Development of an Intense Negative Hydrogen Ion Source with a Wide-Range of External Magnetic Filter Field; Sep. 1994

NIFS-308 T. Hayashi, T. Sato, H.J. Gardner and J.D. Meiss,
Evolution of Magnetic Islands in a Heliac; Sep. 1994

NIFS-309 H. Amo, T. Sato and A. Kageyama,
Intermittent Energy Bursts and Recurrent Topological Change of a Twisting Magnetic Flux Tube; Sep.1994

NIFS-310 T. Yamagishi and H. Sanuki,
Effect of Anomalous Plasma Transport on Radial Electric Field in Torsatron/Heliotron; Sep. 1994

NIFS-311 K. Watanabe, T. Sato and Y. Nakayama,
Current-profile Flattening and Hot Core Shift due to the Nonlinear Development of Resistive Kink Mode; Oct. 1994

NIFS-312 M. Salimullah, B. Dasgupta, K. Watanabe and T. Sato,
Modification and Damping of Alfvén Waves in a Magnetized Dusty Plasma; Oct. 1994

NIFS-313 K. Ida, Y. Miura, S -I. Itoh, J.V. Hofmann, A. Fukuyama, S. Hidekuma, H. Sanuki, H. Idei, H. Yamada, H. Iguchi, K. Itoh,
Physical Mechanism Determining the Radial Electric Field and its Radial Structure in a Toroidal Plasma; Oct. 1994

NIFS-314 Shao-ping Zhu, R. Horiuchi, T. Sato and The Complexity Simulation Group,
Non-Taylor Magnetohydrodynamic Self-Organization; Oct. 1994

NIFS-315 M. Tanaka,
Collisionless Magnetic Reconnection Associated with Coalescence of Flux Bundles; Nov. 1994

NIFS-316 M. Tanaka,
Macro-EM Particle Simulation Method and A Study of Collisionless Magnetic Reconnection; Nov. 1994

NIFS-317 A. Fujisawa, H. Iguchi, M. Sasao and Y. Hamada,
Second Order Focusing Property of 210° Cylindrical Energy Analyzer; Nov. 1994

NIFS-318 T. Sato and Complexity Simulation Group,
Complexity in Plasma - A Grand View of Self- Organization; Nov. 1994

NIFS-319 Y. Todo, T. Sato, K. Watanabe, T.H. Watanabe and R. Horiuchi,
MHD-Vlasov Simulation of the Toroidal Alfvén Eigenmode; Nov. 1994

NIFS-320 A. Kageyama, T. Sato and The Complexity Simulation Group,
Computer Simulation of a Magnetohydrodynamic Dynamo II: Nov. 1994

NIFS-321 A. Bhattacharjee, T. Hayashi, C.C.Hegna, N. Nakajima and T. Sato,
Theory of Pressure-induced Islands and Self-healing in Three-dimensional Toroidal Magnetohydrodynamic Equilibria; Nov. 1994

NIFS-322 A. Iiyoshi, K. Yamazaki and the LHD Group,
Recent Studies of the Large Helical Device; Nov. 1994

NIFS-323 A. Iiyoshi and K. Yamazaki,
The Next Large Helical Devices; Nov. 1994

NIFS-324 V.D. Pustovitov
Quasisymmetry Equations for Conventional Stellarators; Nov. 1994

NIFS-325 A. Taniike, M. Sasao, Y. Hamada, J. Fujita, M. Wada,
The Energy Broadening Resulting from Electron Stripping Process of a Low Energy Au^- Beam; Dec. 1994

NIFS-326 I. Viniar and S. Sudo,
New Pellet Production and Acceleration Technologies for High Speed Pellet Injection System "HIPEL" in Large Helical Device; Dec. 1994

NIFS-327 Y. Hamada, A. Nishizawa, Y. Kawasumi, K. Kawahata, K. Itoh, A. Ejiri, K. Toi, K. Narihara, K. Sato, T. Seki, H. Iguchi, A. Fujisawa, K. Adachi, S. Hidekuma, S. Hirokura, K. Ida, M. Kojima, J. Koong, R. Kumazawa, H. Kuramoto, R. Liang, T. Minami, H. Sakakita, M. Sasao, K.N. Sato, T. Tsuzuki, J. Xu, I. Yamada, T. Watari,
Fast Potential Change in Sawteeth in JIPP T-IIU Tokamak Plasmas; Dec. 1994

NIFS-328 V.D. Pustovitov,
Effect of Satellite Helical Harmonics on the Stellarator Configuration; Dec. 1994

NIFS-329 K. Itoh, S-I. Itoh and A. Fukuyama,
A Model of Sawtooth Based on the Transport Catastrophe; Dec. 1994

NIFS-330 K. Nagasaki, A. Ejiri
Launching Conditions for Electron Cyclotron Heating in a Sheared Magnetic Field; Jan. 1995